Structural basis of mitochondrial dysfunction in response to cytochrome *c* phosphorylation at tyrosine 48

Blas Moreno-Beltrán[a,1], Alejandra Guerra-Castellano[a,1], Antonio Díaz-Quintana[a], Rebecca Del Conte[b], Sofía M. García-Mauriño[a], Sofía Díaz-Moreno[c], Katiuska González-Arzola[a], Carlos Santos-Ocaña[d], Adrián Velázquez-Campoy[e], Miguel A. De la Rosa[a], Paola Turano[b], and Irene Díaz-Moreno[a,2]

[a]Instituto de Investigaciones Químicas, cicCartuja, Universidad de Sevilla–Spanish National Scientific Council (CSIC), 41092 Seville, Spain; [b]Magnetic Resonance Center (CERM), Department of Chemistry, University of Florence, 50019 Sesto Fiorentino, Florence, Italy; [c]Diamond Light Source, Didcot, Oxfordshire OX11 0DE, United Kingdom; [d]Centro Andaluz de Biología del Desarrollo, Universidad Pablo de Olavide–CSIC, 41013 Seville, Spain; and [e]Institute of Biocomputation and Physics of Complex Systems (BIFI), Joint Unit BIFI-Instituto Química-Física Rocasolano (CSIC), Universidad de Zaragoza, 50018 Zaragoza, Spain

Edited by Kara L. Bren, University of Rochester, Rochester, NY, and accepted by Editorial Board Member Harry B. Gray March 8, 2017 (received for review November 1, 2016)

Regulation of mitochondrial activity allows cells to adapt to changing conditions and to control oxidative stress, and its dysfunction can lead to hypoxia-dependent pathologies such as ischemia and cancer. Although cytochrome *c* phosphorylation—in particular, at tyrosine 48—is a key modulator of mitochondrial signaling, its action and molecular basis remain unknown. Here we mimic phosphorylation of cytochrome *c* by replacing tyrosine 48 with *p*-carboxy-methyl-L-phenylalanine (*p*CMF). The NMR structure of the resulting mutant reveals significant conformational shifts and enhanced dynamics around *p*CMF that could explain changes observed in its functionality: The phosphomimetic mutation impairs cytochrome *c* diffusion between respiratory complexes, enhances hemeprotein peroxidase and reactive oxygen species scavenging activities, and hinders caspase-dependent apoptosis. Our findings provide a framework to further investigate the modulation of mitochondrial activity by phosphorylated cytochrome *c* and to develop novel therapeutic approaches based on its prosurvival effects.

cytochrome *c* | mitochondrial dysfunction | nuclear magnetic resonance | phosphorylation | respiratory supercomplexes

Oxidative phosphorylation (OxPhos) relies on the electron transport chain (ETC) to generate the membrane potential that drives ATP synthesis (1). Components of the ETC oxidize substrates to reduce molecular oxygen, thereby producing water. Nevertheless, around 2% of the electrons flowing across the ETC yield reactive oxygen species (ROS) (2). ROS are a source of oxidative stress and act as signaling molecules at low concentrations (3–5). Hindering redox reactions within the distinct ETC membrane complexes (complexes I to V) leads to enhanced ROS production (6). The activity of the ETC is tightly regulated by posttranslational modifications of its components, isoform swapping, and modulation of the equilibria for the association of the membrane protein complexes into supercomplexes (3, 7). Such associations allow substrate channeling while modulating ROS production (3, 7).

Oxidative stress response involves redox signals modulating protein phosphorylation (8). In the ETC, the major phosphorylation targets are NADH:UQ oxidoreductase, cytochrome *c* (C*c*), and cytochrome *c* oxidase (C*c*O) (9). Besides being essential for oxidative respiration (Fig. 1*A*), C*c* acts as a redox regulatory protein within the mitochondrial intermembrane space (10). In addition, C*c* aids in controlling ROS levels by oxidizing superoxide anions (11) and exhibiting peroxidase activity (12); the latter, however, also yields lipid peroxidation (13, 14). Furthermore, C*c* plays a crucial role in programmed cell death, a process that is only partially understood (15–21). In this context, a fraction of C*c* binds and oxidizes cardiolipin (CL) at the internal mitochondrial membrane, thereby facilitating the release of unbound C*c* to the cytoplasm (16, 17). In mammalian cells, extramitochondrial C*c* interacts with apoptosis activating factor 1 (Apaf-1) in the cytoplasm to spark the caspase proteolytic cascade (15). It has recently been shown that C*c* can interact with several other proteins outside the mitochondria in humans and plants (18–21). The similarities between the C*c* signaling networks in both organisms suggest that key programmed cell-death pathways are conserved throughout evolution (22).

C*c* phosphorylation is an alleged modulator of the mitochondrial cell-death pathway (23, 24). Its deregulation is believed to be related to the onset of neurological disorders and cancer (24). Phosphorylation of C*c* is easily reversed by phosphatases, hampering the isolation of the modified protein from tissues (25). Tyr-to-Glu substitutions of C*c*, designed to emulate Tyr48 phosphorylation,

Significance

Cell response to physiological changes and oxidative stress involves the modulation of mitochondrial metabolism. Its dysfunction favors the development of hypoxia-dependent pathologies, including ischemia and cancer. A key modulator of mitochondrial activity is cytochrome *c*, whose cell function is regulated by tyrosine phosphorylation. However, how such modification affects cytochrome *c* structure and function is barely known. Here we report that a phosphomimetic mutant of cytochrome *c* exhibits enhanced dynamics, which could be responsible for the observed differences in cytochrome *c* functionality in oxidative stress and cell death. Thus, phosphorylation of cytochrome *c* becomes a target for further development of robust therapeutic approaches.

Author contributions: B.M.-B., A.G.-C., A.D.-Q., R.D.C., S.D.-M., C.S.-O., A.V.-C., M.A.R., P.T., and I.D.-M. designed research; B.M.-B., A.G.-C., A.D.-Q., R.D.C., S.M.G.-M., S.D.-M., K.G.-A., C.S.-O., A.V.-C., P.T., and I.D.-M. performed research; I.D.-M. contributed new reagents/analytic tools; B.M.-B., A.G.-C., A.D.-Q., R.D.C., A.V.-C., P.T., and I.D.-M. analyzed data; and B.M.-B., A.G.-C., A.D.-Q., M.A.R., P.T., and I.D.-M. wrote the paper.

The authors declare no conflict of interest.

This article is a PNAS Direct Submission. K.L.B. is a Guest Editor invited by the Editorial Board.

Freely available online through the PNAS open access option.

Data deposition: The NMR assignments and coordinates for Y48*p*CMF cytochrome *c* reported in this paper have been deposited in the Biological Magnetic Resonance Data Bank (BMRB entry code 25660) and Protein Data Bank (PDB ID code 2N3Y) databases, respectively.

[1]B.M.-B. and A.G.-C. contributed equally to this work.

[2]To whom correspondence should be addressed. Email: idiazmoreno@us.es.

This article contains supporting information online at www.pnas.org/lookup/suppl/doi:10.1073/pnas.1618008114/-/DCSupplemental.

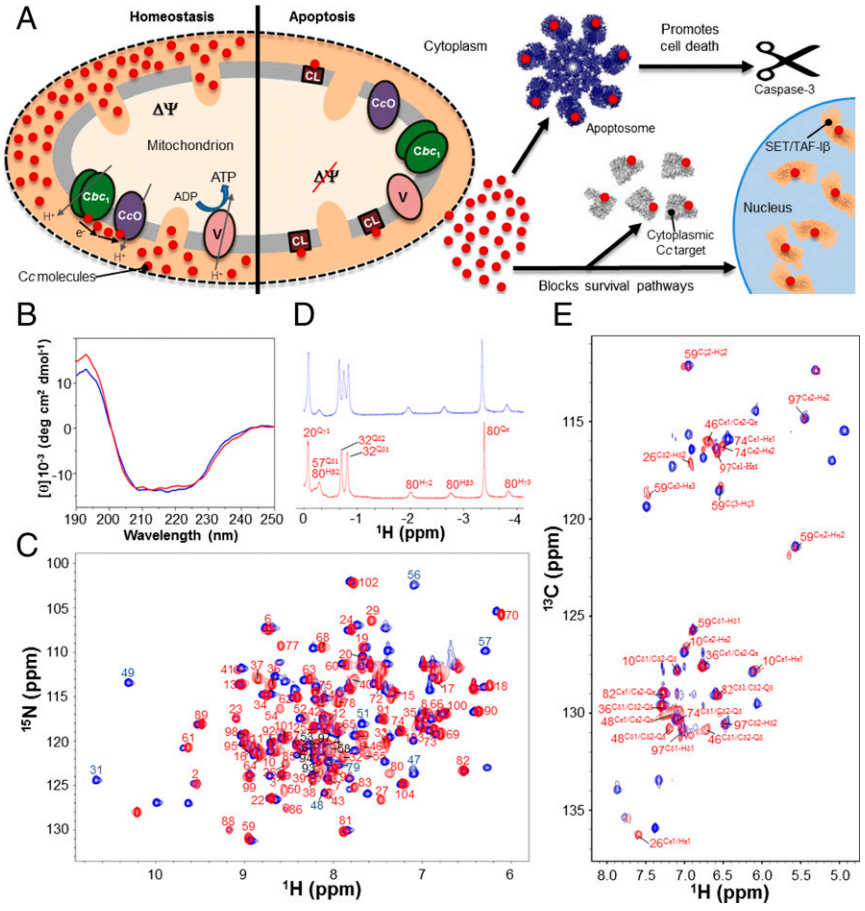

Fig. 1. Control of human cell fate by the Cc-based signalosome, and biophysical and structural characterization of the Y48*p*CMF variant of Cc. (*A*) Diagram of the role of Cc in homeostasis and apoptosis. (*A*, *Left*) Under homeostatic conditions, Cc (red circles) transfers electrons from the cytochrome bc_1 complex (Cbc_1) to the cytochrome *c* oxidase complex (CcO). (*A*, *Right*) Upon apoptotic stimuli, Cc is released to the cytosol to induce apoptosome formation and block prosurvival pathways. A portion of Cc remains bound to cardiolipin. (*B*) Far-UV CD spectra of the reduced forms of WT (blue) and Y48*p*CMF Cc (red). The same color code is maintained in the following panels. (*C*) Superimposition of the ^{1}H–^{15}N HSQC spectra of uniformly ^{15}N-labeled forms of WT and Y48*p*CMF Cc. Backbone amide resonances of Y48*p*CMF Cc are labeled in red and black. Particular amide resonances of WT Cc are labeled in blue. (*D*) Detailed view of the ^{1}H NMR spectra of WT and Y48*p*CMF Cc at negative ppm values. Resonances for Met80 side-chain protons are shown for both Cc species. Assigned signals of all residues within this region are displayed for Y48*p*CMF Cc. The extra signal of WT Cc corresponds to the $Q\delta_1$ protons of Ile53. (*E*) Superimposition of the aromatic region of the ^{1}H–^{13}C HSQC spectra of WT and Y48*p*CMF Cc acquired in ^{13}C natural abundance. Assigned aromatic resonances of Y48*p*CMF Cc are displayed in red.

impair both the electron donation to CcO and the activation of caspase-9 mediated by Apaf-1 in vitro (26, 27). Notably, nitration of this residue also hinders the ability of Cc to activate Apaf-1 (28–30). Thus, these posttranslational modifications alter both mitochondrial and cytoplasmic functions of Cc. Tyr48 phosphorylation also affects the physical-chemical properties of Cc, such as its alkaline transition and midpoint reduction potential (E_0) (27, 31). Understanding the origin of these effects and how they affect Cc activities requires solving the 3D conformation of the phosphorylated species. However, deciphering the effects of Tyr48 phosphorylation on the structure and dynamics of Cc is highly challenging because of its reactivity toward phosphatases. Indeed, no atomic-resolution structure has been reported for either phosphorylated Cc or any reliable mimic mutant.

Here we have elucidated the structure of a phosphomimetic Cc variant in which Tyr48 is replaced by the synthetic, noncanonical amino acid *p*-carboxy-methyl-L-phenylalanine (*p*CMF). We show that such replacement induces local perturbations of the Cc structure and enhanced internal dynamics of the mutation's surroundings. We used biochemical assays to show that the Y48*p*CMF mutation impairs Cc channeling between cytochrome bc_1 (Cbc_1) and CcO, enhances peroxidase activity, and induces an antiapoptotic function of Cc.

Results

Phosphorylation of Tyr48 Induces Local Structural Changes in Cytochrome *c*. To understand how phosphorylation affects the structure of human Cc, we tackled the challenge of fully characterizing the phosphomimetic mutant Y48*p*CMF Cc in its reduced form, which is the redox state of Cc donating electrons to CcO in homeostasis and is essential for its apoptotic activity, because Cc becomes highly reduced upon its release from the mitochondria to the cytosol (32). Y48*p*CMF Cc maintains the overall secondary structure and global fold of wild-type (WT) Cc, as inferred from circular dichroism (CD) (Fig. 1*B*) and ^{1}H–^{15}N heteronuclear single-quantum correlation (HSQC) NMR spectra (Fig. 1*C*), respectively. Also, the native heme axial coordination was preserved, as indicated by 1D ^{1}H NMR data (Fig. 1*D*). The NMR spectra of reduced Y48*p*CMF Cc were extensively assigned: Triple-resonance experiments (*SI Appendix*, Table S1) allowed us to detect and assign 91 backbone amide signals and the sequential connectivities for most residues of the protein. Aliphatic side-chain signals were assigned using 3D HBHA(CO)NH and 3D HCCH-total correlation spectroscopy (TOCSY) experiments, leading to the assignment of most (96.4%) of the side-chain proton resonances. The ^{15}N–H resonance of *p*CMF48 was undetectable because the residue was not ^{15}N-enriched. Four proline residues (Pro30, Pro44, Pro71, and Pro76) interrupt the sequential HN–HN connectivity. Additionally, in contrast to WT Cc, we could not detect the amide protons of the Thr49, Ala51, Gly56, and Ile57 residues. However, the WT spectra only had four amide protons that could not be detected (Gly1, Glu21, Thr28, and Gly84) under similar experimental conditions. Further, in contrast to WT Cc, the signals from Asn31, Gly45, and Ser47 in *p*CMF48 Cc were significantly weaker than the rest. The largest chemical-shift perturbations for backbone amides induced by the modified residue at position 48 are confined to nearby residues (*SI Appendix*, Fig. S1).

Assigning ^{1}H resonances to the heme substituents and ^{1}H (and ^{13}C) signals to the aromatic side chains was required for analyzing additional 2D maps (i.e., COSY and ^{1}H–^{15}N NOESY) (*SI Appendix*, Table S1). Assignment of the $C\delta_1$, $C\delta_2$, $C\varepsilon_1$, and $C\varepsilon_2$ aromatic signals from the *p*CMF48 side chain required the acquisition of an aromatic ^{1}H–^{13}C HSQC spectrum recorded in a

natural abundance of ^{13}C (Fig. 1*E*). The assignment of the *p*CMF48 side-chain signals involved the complete assignment of the 2D ^{1}H–^{15}N NOESY.

Numerous residues (Val20 to Asn31, Thr40 to Trp59, and Ile75 to Glu90) displayed signals attributable to a second, minor protein conformation, which had a 1:10 ratio in intensity. Hereafter, only the major form was considered for structure calculations.

We assigned 96% of all the ^{1}H signals for the major form. Structural information derived from 2D and 3D NOESY maps supported the presence of five α-helical regions (labeled α_1 to α_5) with typically strong HN–HN (*i*, *i*+1), medium-range Hα–HN (*i*, *i*+3), and Hα–HN (*i*, *i*+4) interresidual NOEs. These regions spanned the sequence stretches Val3 to Lys13, Ala50 to Asn54, Glu61 to Glu69, Pro71 to Tyr74, and Lys88 to Thr102, resembling those in the NMR structure of reduced WT C*c* (33). In total, we observed and assigned 2,176 meaningful NOEs, corresponding to 20.8 relevant restraints per residue on average (*SI Appendix*, Fig. S2). The 71 ϕ and 71 ψ dihedral-angle constraints were derived from ^{15}N, $^{13}C'$, $^{13}C\alpha$, $^{13}C\beta$, and Hα chemical shifts, using TALOS+ (34). The heme moiety was included in the calculations as previously reported for WT cytochromes (35, 36), assuming an intact heme iron coordination as supported by X-ray absorption spectroscopy (XAS) data (next section).

Two hundred structures were calculated by CYANA (37), and the 20 structures with the lowest target-function (TF) value were selected to form a representative family. The range of TF values was 0.38 to 0.98 $Å^2$, highlighting the high accuracy between calculated and experimental distances. Further refinement of the 20 lowest TF structures involved restrained energy minimization and restrained molecular dynamics (RMD) computations. A final restrained energy minimization was carried out on the structure with the lowest root-mean-square deviation (rmsd) from the average for each of the 20 trajectories. The overall quality of the 20 lowest TF ensembles was good, according to the PROCHECK G factor (38), MolProbity clashscores (39), and other structural quality indicators (*SI Appendix*, Table S2). Most residues were in the Ramachandran plot favored regions, whereas Cys14, Cys17, His18, Val20, Lys37, and Asn70 were in the generously allowed ones, as also observed for the solution structure of WT C*c* (33, 40). Cys14, Cys17, and His18 are covalently bonded to the heme moiety, thereby straining their backbone conformation, as already described for *c*-type cytochromes (35, 36). As an additional control, we performed 20-ns unrestrained molecular dynamics (MD) simulations of the final minimized conformers without any geometrical restraint. The rmsd for the main-chain atoms was about 1.55 Å at the plateau, hardly drifting (0.122 pm·ns^{-1}), as expected for a stable structure (*SI Appendix*, Fig. S3).

The overall fold of Y48*p*CMF C*c* is very similar to that of the WT species (*SI Appendix*, Fig. S4), with rmsd values for the backbone nuclei of 1.67 ± 1.01 Å (Fig. 2 *A* and *B*). However, the two structures differ in the mutation-containing loop Ω_{NY} (residues 40 to 57; Fig. 2*B*). This is consistent with the chemical-shift differences (*SI Appendix*, Fig. S1) and the rmsd between the NMR solution structure of WT C*c* [Protein Data Bank (PDB) ID code 1J3S] (33) and the refined lowest-TF Y48*p*CMF C*c* (*SI Appendix*, Fig. S5*A*). An increased dynamics in the Ω_{NY}-loop has recently been observed in the G41S variant of C*c* (42). The Ω_{NY}-loop (also known as foldon V) and helix α_2 constitute the less-stable folding unit of C*c* (43). Unlike Tyr48 in the WT species, the *p*CMF48 residue presents a very low number of ^{1}H–^{1}H NOEs (*SI Appendix*, Fig. S2) and a high rmsd value within the family (Fig. 2*C* and *SI Appendix*, Fig. S5*B*). A decrease in the number of detectable NOEs can generally be attributed to either a partial assignment of the residue or an increased internal mobility. In our case, the highly dynamic behavior of the *p*CMF48 residue was confirmed from further analysis of internal motions within the nanosecond-to-picosecond timescale (see below).

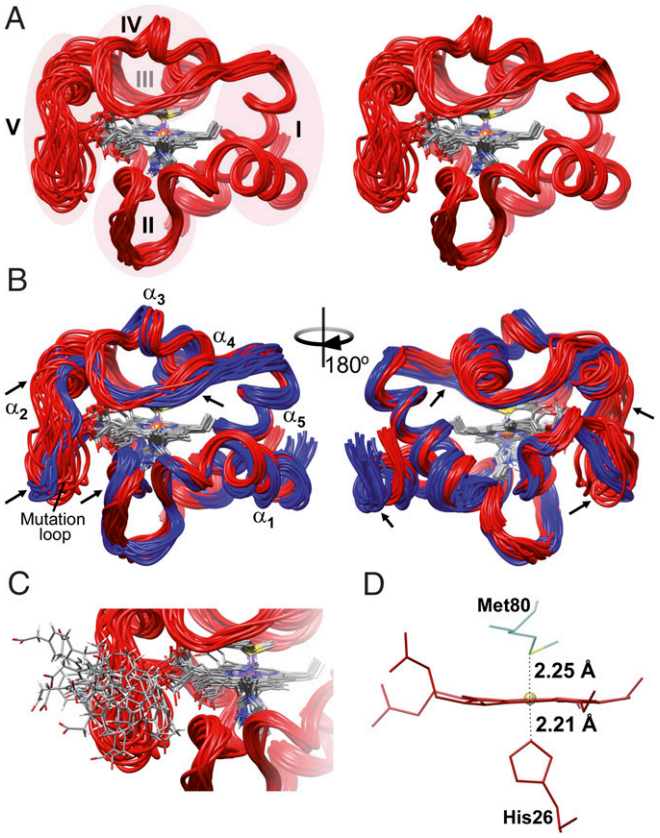

Fig. 2. NMR solution structure of the Y48*p*CMF variant of C*c*. (*A*) Stereo-view ribbon representation of the 20 best conformers of Y48*p*CMF C*c*. Heme group atoms are displayed for all conformers. Ribbons are colored in red, whereas atoms from the heme group are colored following the CPK (Robert Corey, Linus Pauling, and Walter Koltun) color scheme. Foldons of Y48*p*CMF C*c* are shadowed and marked with roman numerals, except for foldon III, which is located behind foldon IV. (*B*) Comparison between the NMR solution structures of WT C*c* (PDB ID code 1J3S) (33) and Y48*p*CMF C*c* (this work). The ribbon for WT C*c* is in blue. The five α-helices of both C*c* species, as well as the mutation-containing loop of Y48*p*CMF C*c*, are marked. Arrows point to the regions on the Y48*p*CMF C*c* ribbon with substantial structural changes compared with the WT form. (*C*) Detailed view of the loop harboring the *p*CMF48 residue. *p*CMF48 atoms follow the CPK color scheme. Protein structures are presented by UCSF Chimera software (41). (*D*) Detail of the heme group and axial ligands. Labels display iron-to-axial ligand distances for the Y48*p*CMF mutant obtained from the EXAFS analysis (*SI Appendix*, Fig. S5).

Other regions of the Y48*p*CMF C*c* structure that differed from those of WT C*c* belong to the 19 to 36 Ω_G-loop (part of foldon II) and the 71 to 85 Ω_R-loop (foldon IV) comprising Met80 and helix α_4. The rmsd values for backbone atoms of residues from Val20 to Gly29 of Y48*p*CMF C*c* are higher (2.75 ± 1.50 Å) than those for the same residues of WT C*c* (*SI Appendix*, Fig. S5*A*). In the second loop, the observed differences are mainly restricted to side chains. In fact, the rmsd values for backbone and heavy atoms are 1.18 ± 0.37 and 1.77 ± 0.71 Å, respectively. Residues included in the Ω_R-loop indeed displayed a double conformation, suggesting the presence of conformational equilibria (*SI Appendix*, Fig. S5*A*).

The ensemble of structures for Y48*p*CMF C*c* is very precise, except for residues surrounding the mutation. The backbone rmsd from the mean is 0.89 ± 0.01 Å for the whole protein and drops to 0.53 ± 0.12 Å when the mutation surroundings are excluded (residues 40 to 57) (*SI Appendix*, Fig. S5*B*). As expected, the highest rmsd values correspond to the 40 to 57 Ω_{NY}-loop and the nearby residues Val20 to Gly29 in loop Ω_G, whose global backbone

rmsd values were 1.79 ± 0.53 and 0.78 ± 0.23 Å, respectively. These segments also exhibited a larger conformational variability in their secondary structure elements along the MD trajectory (*SI Appendix*, Fig. S3 *B* and *C*). High rmsd values along the Val20-to-Gly29 stretch are typical in C*c* homologs (35, 36). They are also consistent with NMR signals revealing secondary conformations for the His26-to-Pro30 stretch. Moreover, the nearby Asn31 amide signal is weak, suggesting high mobility. Notably, all these residues contact the Ω_{NY}-loop, comprising the Y48*p*CMF mutation.

Further, the highest rmsd values mapped to the Ω_{NY}-loop. Consistently, signals from this region undergo a drastic reduction in their ^{1}H–^{1}H NOE cross-peaks. The intensities of the amide signals of Gly45 and Ser47 in Y48*p*CMF C*c* were severely decreased, whereas those from Thr49, Ala51, Gly56, and Ile57 were undetectable. The Ω_{R}-loop also contains some residues with high rmsd values (*SI Appendix*, Fig. S5*B*). The global rmsd value for backbone atoms of the 71 to 85 Ω_{R}-loop is 0.76 ± 0.20 Å. Notably, the end of the Ω_{R}-loop shows high rmsd values in WT cytochromes (35, 36).

Heme Iron Coordination Is Insensitive to Tyr48 Phosphorylation. We tested the effects of the mutation on the heme iron coordination environment and the axial coordination restraints used in our structure computations by using X-ray absorption spectroscopy, studying both WT and Y48*p*CMF species (Fig. 2*D* and *SI Appendix*, Fig. S5 *C*–*F*). The absorption spectra of the two proteins are almost identical. The X-ray absorption near-edge structure regions of the absorption spectra for both proteins are superimposed (*SI Appendix*, Fig. S5*C*). The absence of any shift in the energy position of the absorption edge indicates that the mutation did not affect the electron density at the Fe center.

Likewise, the extracted extended X-ray absorption fine structure (EXAFS) signals of the WT and Y48*p*CMF C*c* species were highly similar. However, small differences in high wave vector (k) values can be observed (*SI Appendix*, Fig. S5*D*), as well as in the slightly lower amplitude of the Y48*p*CMF protein. Whereas the corresponding Fourier transforms are also very similar (*SI Appendix*, Fig. S5*E*), the amplitude of the first peak is lower and broader in the Y48*p*CMF C*c* species, suggesting a larger degree of disorder. The dynamic disorder for the two proteins should be similar, as the measurements were performed at cryogenic temperatures in both cases. Hence, the differences in disorder are due to a larger static disorder in Y48*p*CMF C*c*. The main scattering paths contributing to this peak originate from the four nitrogen atoms of the porphyrin ring, although contributions of the nitrogen and sulfur axial ligands have also been included. The fit to the data requires the addition of the paths involving the eight porphyrin carbons closest to the iron atom, beyond the first coordination sphere. In addition, the multiple scattering paths involving these atoms were also included. Fits were performed in R space but also reproduced the spectra well in q space (*SI Appendix*, Fig. S5*F*). The parameters obtained from the best fit to the data revealed that the distances between the iron atom and its first coordinating ligands are insensitive to the Y48*p*CMF mutation (*SI Appendix*, Table S3). Specifically, the distances from the iron center to the axial S ligand are 2.26 ± 0.001 and 2.25 ± 0.001 Å in the WT and phosphomimetic mutant species, respectively (Fig. 2*D*). Data analyses also showed that the value for the Debye–Waller factor corresponding to the path involving the four porphyrin nitrogen atoms increased from 0.0012 ± 0.0006 $Å^2$ in the WT species to 0.003 ± 0.001 $Å^2$ in the Y48*p*CMF mutant. These data are consistent with the preserved chemical-shift pattern of the iron axial ligands and heme substituents observed in 1D ^{1}H NMR (Fig. 1*D*), which have been reported to be sensitive indicators of the heme iron electronic structures (35, 36). The pattern of the observed NOEs for the heme substituents also supports an overall intact heme pocket, with the exception of the mutation site. Still, the ensemble of structures shows a small change in the orientation of Phe82 with respect to the porphyrin ring (*SI Appendix*, Fig. S6).

Phosphorylation of Tyr48 Enhances Internal Mobility in Cytochrome *c*. NMR relaxation measurements were performed to evaluate the dynamics of WT and Y48*p*CMF C*c*. The Y48*p*CMF substitution slightly affected both relaxation rate (R_1 and R_2) parameters (*SI Appendix*, Table S4). The rotational correlation time of the phosphomimetic mutant (6.96 ± 0.02 ns) was higher than that of the WT form (6.33 ± 0.02 ns), in agreement with the small increase (p_{nul} values of $\sim 10^{-251}$, where p_{nul} is the probability for the null hypothesis being the right one) in the average gyration radius, from 12.95 ± 0.07 to 13.04 ± 0.06 Å, as calculated by MD. Indeed, phosphorylation can alter protein dynamics at different timescales and cause conformational rearrangements, such as the formation of secondary conformations (44, 45).

Comparing R_1, R_2, and heteronuclear NOE (HetNOE) relaxation measurements recorded on the two proteins revealed that the Ω_{NY}-loop of Y48*p*CMF C*c* exhibits a high mobility in the

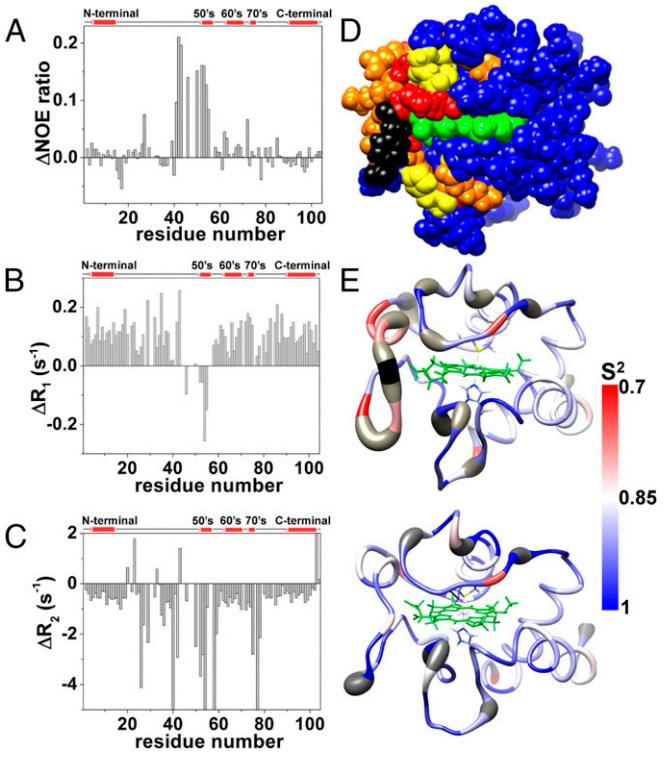

Fig. 3. Relaxation NMR measurements and dynamic properties of WT and Y48*p*CMF C*c*. (*A*–*C*) Differences in heteronuclear NOE (*A*), relaxation rate R_1 (*B*), and relaxation rate R_2 (*C*) between the experimental values for the reduced forms of WT and Y48*p*CMF C*c*, plotted as a function of the residue number. Gaps in data result from overlapping resonances, broadened resonances beyond the detection limit, and unassigned resonances. A scheme of the secondary structure elements is included (*Top*). (*D*) Map of the Y48*p*CMF C*c* residues colored according to their dynamic properties. Affected residues in the heteronuclear NOE and relaxation rate R_2 parameters are colored in yellow and orange, respectively. Residues with backbone amide resonances that are undetectable in the ^{1}H–^{15}N HSQC spectrum of Y48*p*CMF C*c* but detectable in the ^{1}H–^{15}N HSQC spectrum of WT C*c* are colored in red. *p*CMF48 is shown in black, and the heme group is in green. Unaffected, unassigned, and proline residues are in blue. (*E*) Internal mobility comparison between Y48*p*CMF and WT C*c*. S^2-order parameter values per residue for Y48*p*CMF (*Upper*) and WT (*Lower*) C*c* are represented on the respective NMR ribbon structures using a blue–red scale. Undetectable backbone resonances are in gray. Heme atoms are in green, with the axial ligands depicted as sticks.

picosecond-to-nanosecond timescale (Fig. 3). Indeed, the Gly41-to-Lys55 segment showed a drastic drop of HetNOE values in the mutant species (Fig. 3*A*). Further, the amide R_1 rates for the sequence stretch of Tyr46 to Lys55 in Y48*p*CMF C*c* differ from those in WT C*c* (Fig. 3*B*). In addition, R_2 analysis reveals three regions undergoing conformational exchange in the microsecond-to-millisecond timescale: His26 to Thr28, Thr40 to Trp59, and Ile75 to Thr78 (Fig. 3*C*). This behavior agrees with the reduced intensity or lack of detection of the amide signals belonging to these stretches, compared with the WT form. Furthermore, some regions within the protein displayed signals corresponding to double conformations in the 2D ^{1}H NOESY spectra—namely Val20 to Asn31, Thr40 to Trp59, and Ile75 to Glu90—indicating the presence of conformational equilibria between two different structures occurring on a slow timescale with respect to the NMR chemical shift. This dynamics involves residues located in a defined region surrounding the noncanonical amino acid (Fig. 3*D*). Altogether, the NMR relaxation measurements of Y48*p*CMF C*c* agree with the per-residue S^2-order parameter values computed with TENSOR (46) (Fig. 3*E*).

Hydrogen–deuterium exchange experiments showed that a common core region is protected from solvent amide–hydrogen exchange in both C*c* species. Nevertheless, a substantial number of amides become unprotected in *p*CMF48 C*c* (*SI Appendix*, Fig. S7). The newly accessible amide protons in the phosphomimetic mutant (Gly29, Gly37, Arg38, Thr40, Gln42, and Trp59) are located in the surroundings of *p*CMF48 and the nearby Ω_G-loop, in agreement with their high mobility in the microsecond-to-millisecond timescale.

Tyr48 Phosphorylation Modulates the Interaction of Cytochrome *c* with Its Mitochondrial Partners in the Electron Transfer Chain. C*c* carries electrons from C*bc*$_1$ to C*c*O within the ETC. To elucidate more details about the process, we analyzed the molecular recognition between the soluble N-terminal domain of plant cytochrome c_1 (Cc_1) or bovine C*c*O and the phosphomimetic human Y48*p*CMF C*c*. The human and plant N-terminal domains of Cc_1 have a 62% overall sequence identity and similar charge distributions on their molecular surfaces (47), whereas the bovine and human C*c*O are evolutionarily related proteins, with 91 and 96% sequence identity and homology, respectively.

Two binding sites for human and plant C*c* on plant Cc_1 have been recently reported (47, 48). The proximal site is located near the heme moiety and is compatible with electron transfer, whereas the distal site lies far from the heme group and probably constitutes a local energy minimum of the encounter ensemble.

To test how Tyr48 phosphorylation affects the conformation of the Cc_1–C*c* complex, we recorded ^{1}H–^{15}N HSQC spectra upon titration of ^{15}N-labeled reduced C*c* with unlabeled reduced Cc_1. Several amide signals exhibited significant chemical-shift perturbations (CSPs), thus indicating a fast exchange rate within the NMR timescale (Fig. 4 *A* and *B*). Average amide CSPs ($\Delta\delta_{avg}$) were larger than 0.075 ppm for 11 residues: Gln16, Lys27, Gly29, Ala50, Lys55, Ile58, Lys72, Gly77, Met80, Ile81, and Val83 (Fig. 4*B*). The fits of CSPs along the titration suggested that Cc_1 binds two Y48*p*CMF C*c* molecules, as previously found with the WT C*c* species (47, 48) (Fig. 4*C*). Using NMR spectroscopy, the dissociation constant (K_D) values for the Cc_1–Y48*p*CMF C*c* complex were estimated to be 0.6 and 102 μM for the proximal and distal binding sites, respectively. All of the perturbed residues, except Lys55 and Ile58, surround the heme crevice, as previously described for the interaction between WT C*c* and Cc_1 (47, 48) (Fig. 4*D*). In fact, this region constitutes a very well conserved interaction surface in *c*-type cytochromes (49–52). Lys55 and Ile58, in turn, are located in the Ω_{NY}-loop, which undergoes a conformational exchange in free Y48*p*CMF C*c* (Fig. 4*D*). In addition, significant CSPs ($\Delta\delta_{avg} \geq 0.05$ ppm) were detected for Lys7, Lys13, His26, Lys39, Ala43, Thr78, Lys86, Lys88, and Glu89. Interestingly, Lys8, Lys13, Lys27,

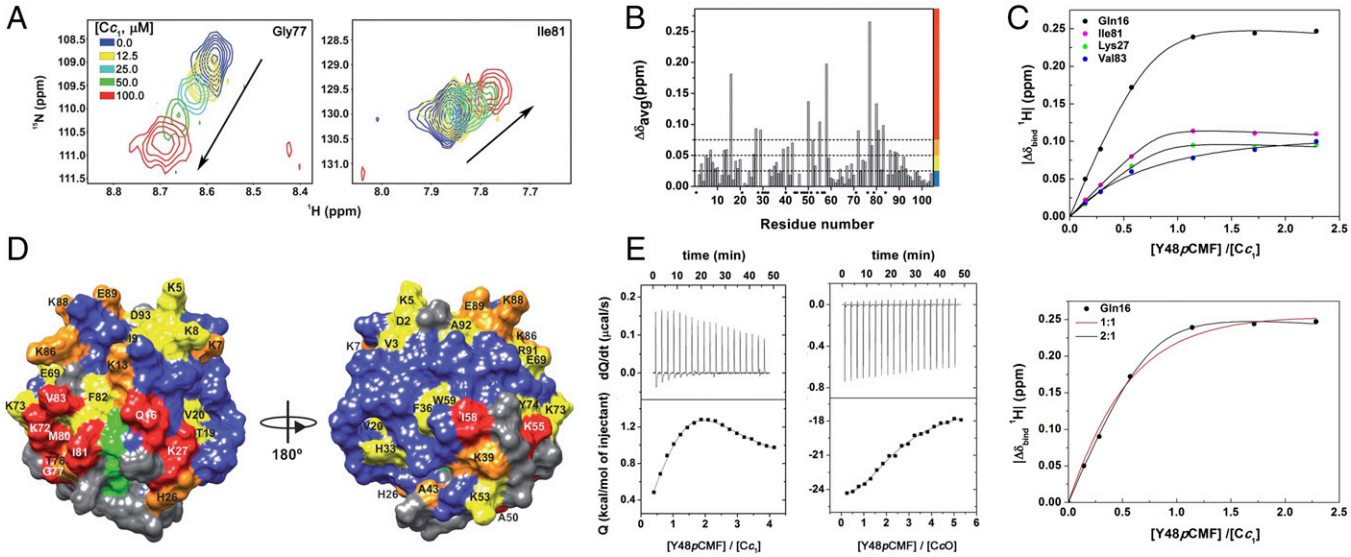

Fig. 4. Binding assays between Y48*p*CMF C*c* and its respiratory partners. (*A*) Overlay of selected residues of ^{1}H–^{15}N HSQC spectra of ^{15}N-labeled Y48*p*CMF C*c* along with titration with Cc_1. Signals corresponding to different titration steps are colored according to the code indicated. (*B*) Plot of chemical-shift perturbations of ^{15}N-labeled Y48*p*CMF C*c* as a function of residue number. Proline and nonassigned residues are marked by asterisks. Color bars stand for the $\Delta\delta_{avg}$ categories: insignificant $\Delta\delta_{avg} < 0.025$ ppm, blue; small $0.025 \leq \Delta\delta_{avg} < 0.050$ ppm, yellow; medium $0.050 \leq \Delta\delta_{avg} < 0.075$ ppm, orange; and large ≥ 0.075 ppm, red. (*C*, *Upper*) Curves representing the best global fit of several amide signals in the ^{1}H dimension to a 2:1 ratio for the Y48*p*CMF C*c*–Cc_1 binding model with two different global K_D values. (*C*, *Lower*) Binding curves of Gln16. Lines represent the best fit to 1:1 (red) and 2:1 (black) binding models. (*D*) CSP map of reduced Y48*p*CMF C*c* upon addition of reduced Cc_1 at a 1:1 ratio. Residues are colored according to $\Delta\delta_{avg}$ categories, as indicated in *B*. Proline and nonassigned residues are in gray. (*E*) ITC measurements of the Y48*p*CMF C*c*–Cc_1 and Y48*p*CMF C*c*–C*c*O complexes in their reduced states. Experimental data were fitted to a 2:1 binding model. Thermograms (*Upper*); binding isotherms (*Lower*).

Lys72, and Lys86 also experienced large CSPs, as previously reported for the interaction between WT Cc and Cc_1 (47, 48).

To obtain further data on the binding affinity and stoichiometry of the interaction between the two redox proteins, isothermal titration calorimetry (ITC) experiments were performed on both redox states. The isotherms obtained by titrating reduced Y48*p*CMF Cc with reduced Cc_1 are displayed (Fig. 4*E*, *Left*). For the interaction between Cc and Cc_1, the isotherm clearly shows two components with opposite signs in their respective enthalpy terms, thereby indicating the presence of two binding sites, in agreement with the NMR data herein presented and previous reports on the WT species (47, 48). Indeed, all data fit a model with two independent binding sites in the corresponding Cc partner (*SI Appendix*, Table S5). The interaction between Y48*p*CMF Cc and Cc_1 was entropy-driven. At pH 7.4, the K_D value at the proximal site was half that observed for WT Cc, whereas that at the distal site was four times higher (*SI Appendix*, Table S5). This could be ascribed to the extra negative charge at position 48, which alters the surface electrostatic potential of the hemeprotein (*SI Appendix*, Fig. S8). Both Cc_1–Y48*p*CMF Cc and Cc_1–Cc complexes in their oxidized states showed similar thermodynamic and equilibrium parameters at both acidic and basic pH values. The only exception was the K_D value for the oxidized Cc_1–Y48*p*CMF Cc complex, at the proximal site of Cc_1, which was approximately four times lower than that for the oxidized Cc_1–WT Cc adduct at pH 8.5. ITC measurements of the oxidized Cc_1–Y48*p*CMF Cc complex were not run at pH 7.4 because the pK_a for the alkaline transition, which is specific to the ferric state (53), shifts to neutral pH upon Tyr48 phosphorylation (31). Hence, the WT and phosphomimetic forms of oxidized Cc can differ in their sixth axial ligand at pH 7.4 (*SI Appendix*, Table S5).

In addition, we analyzed the binding affinity of the cross-complex between the reduced species of bovine CcO and human Y48*p*CMF Cc by ITC. The isotherm inflection point lies at a 2:1 Y48*p*CMF-Cc:CcO ratio, thereby indicating the presence of two binding sites on CcO, as previously found for WT Cc (47, 54, 55). The best fit was achieved when the model used distinct K_D values for the two independent binding sites (*SI Appendix*, Fig. S9). The resulting isotherms likewise fit to such a model, yielding different micromolar-ranging K_D values (Fig. 4*E*, *Right* and *SI Appendix*, Table S6) and enthalpy-driven interactions. Both the CcO proximal and distal sites had lower affinities for Y48*p*CMF Cc than the WT species, as previously reported (47) (*SI Appendix*, Table S6). Altogether, these data agree with previous steady-state kinetic analysis that demonstrated a binding model with more than one molecule of Cc per molecule of Cbc_1 (56) and with kinetic-based models that proposed the existence of alternative, nonproductive binding sites for horse Cc in bovine CcO (55). In addition, direct binding studies performed by gel filtration between several mammalian Ccs and bovine CcOs evidenced a 2:1 stoichiometry, in which Cc bound to a first site with a dissociation constant within the nanomolar range and to a second site with less affinity (54).

To assess the functional ability of Y48*p*CMF Cc to reduce respiratory complex IV, we tested the CcO activity of isolated complex IV or Cc-free mitochondria (ΔCc) from yeast cells grown with glucose as a carbon source (Fig. 5*A* and *SI Appendix*, Fig. S10*A*). In both cases, the Cc oxidation rate was at least twofold higher with Y48*p*CMF Cc than with WT Cc, thereby suggesting that Tyr48 phosphorylation enhances the ability of Cc to donate electrons to complex IV. Direct measurements of O_2 consumption were consistent with such data (*SI Appendix*, Fig. S10*B*). Interestingly, the CcO activity was positively regulated by the human membrane proteins hypoxia-inducible domain family members 1A and 2A (HIGD1A and HIGD2A), which promote cell survival under hypoxia. HIGD2A was successfully expressed in cell-free expression systems combined with *n*-dodecyl-β-D-maltoside, as previously reported for HIGD1A (57) (*SI Appendix*, Fig. S11 *A*–*C*). HIGD1A significantly increased the rate of CcO-catalyzed oxidation of Y48*p*CMF Cc (Fig. 5*B*), as reported for WT Cc (58). Strikingly, HIGD2A induced an even stronger positive effect than HIGD1A (Fig. 5*B*). Nevertheless, the HIGD-dependent increase in CcO activity was slightly lower with Y48*p*CMF Cc (Fig. 5*B*). This may be due to HIGD-dependent changes in either the complex IV affinity toward Cc or the restraints of Cc diffusion (channeling) from Cc_1 to complex IV. A direct Cc–HIGD interaction can also not be excluded.

To confirm the HIGD-mediated regulation of the CcO activity in a cellular context, we isolated mitochondria from different yeast strains grown either with glucose (YPD medium), which supports fermentation and respiration, or with the nonfermentable carbon sources lactate and galactose (YP-Gal) (59). Under both metabolic conditions, the isoformic respiratory supercomplex factors 1 (Rcf1, formerly Aim31) and 2 (Rcf2, formerly Aim38) are constitutively expressed (Fig. 5*C*, *Inset*), in agreement with their role in CcO activity and supercomplex stability (59–61). Rcf1 is a yeast ortholog of the human HIGD1A and HIGD2A proteins, whereas Rcf2 is specific to yeast. The external membranes of isolated mitochondria were then permeabilized to allow the entry of exogenous WT or Y48*p*CMF Cc. Under these conditions, mitochondria isolated from a yeast strain deficient in both Rcf1 and Rcf2 (ΔRcf1/2), as verified by Western blot, displayed an endogenous CcO activity lower than that isolated from WT yeast (WT_{Rcf}), no matter which type of exogenous hemeprotein—WT or Y48*p*CMF Cc—was used for supplementation (Fig. 5*C*). This indicates that Rcf1 and Rcf2 act as positive modulators of CcO activity, similar to human HIGD proteins. In mitochondria isolated from yeast grown with nonfermentable carbon sources, the Rcf-mediated increase in CcO activity was less prominent when Y48*p*CMF Cc rather than WT Cc was added as an exogenous electron donor, in agreement with the in vitro behavior of isolated proteins (Fig. 5*B*). This suggests that Tyr48 phosphorylation makes Cc less sensitive to the enhancer mechanism of the Rcf proteins and/or to the ability of Rcfs to stabilize the Cbc_1–CcO supercomplexes (Fig. 5*C*). In fact, Rcf1 and Rcf2 promote the supercomplex assembly, preferably in mitochondria from yeasts grown in a respiratory-based medium (Fig. 5*D* and *SI Appendix*, Fig. S11*D*). This is especially remarkable when comparing the band intensities in an anti–COX-II immunoblot (Fig. 5*D*). Note that such OxPhos supercomplexes could show a certain degree of heterogeneity in their composition, because the gene transcription of COX-Va and COX-Vb—which encode for two CcO isoforms—is repressed and active, respectively, in the aerobic-to-anaerobic metabolic transition (62). Moreover, the faint band pattern of ΔRcf1/2 strains grown in YPD medium on blue native (BN)/PAGE corresponds to supercomplexes, thus suggesting that other factors may contribute to their assembly (Fig. 5*D* and *SI Appendix*, Fig. S11*D*).

Altogether, our data suggest that phosphorylation of Cc at Tyr48 modulates the mitochondrial ETC (Fig. 5*E*). Such a post-translational modification allows a fast adaptation of the hemeprotein function to changing cell conditions. The population of Cbc_1–CcO supercomplexes is less prominent in the presence than in the absence of glucose, although Rcf proteins are still expressed. In any case, Cc channeling from Cbc_1 toward CcO is impaired. At a physiological pH, Tyr48 phosphorylation thus favors binding of Cc to the proximal rather than to the distal site of Cc_1. Under respiration-based growth, the Rcf proteins preferably associate directly with the OxPhos supercomplex, bridging Cbc_1 and CcO. However, the weaker Y48*p*CMF Cc–CcO binding, along with the loss of the distal site on Cc_1 due to phosphorylated Cc, impairs the channeling of Cc molecules that functionally connects Cbc_1 with CcO, which has been proposed to occur with WT Cc (47, 48). As a consequence, Y48*p*CMF Cc is less efficient than WT Cc as an electron carrier toward CcO in the context of OxPhos supercomplexes.

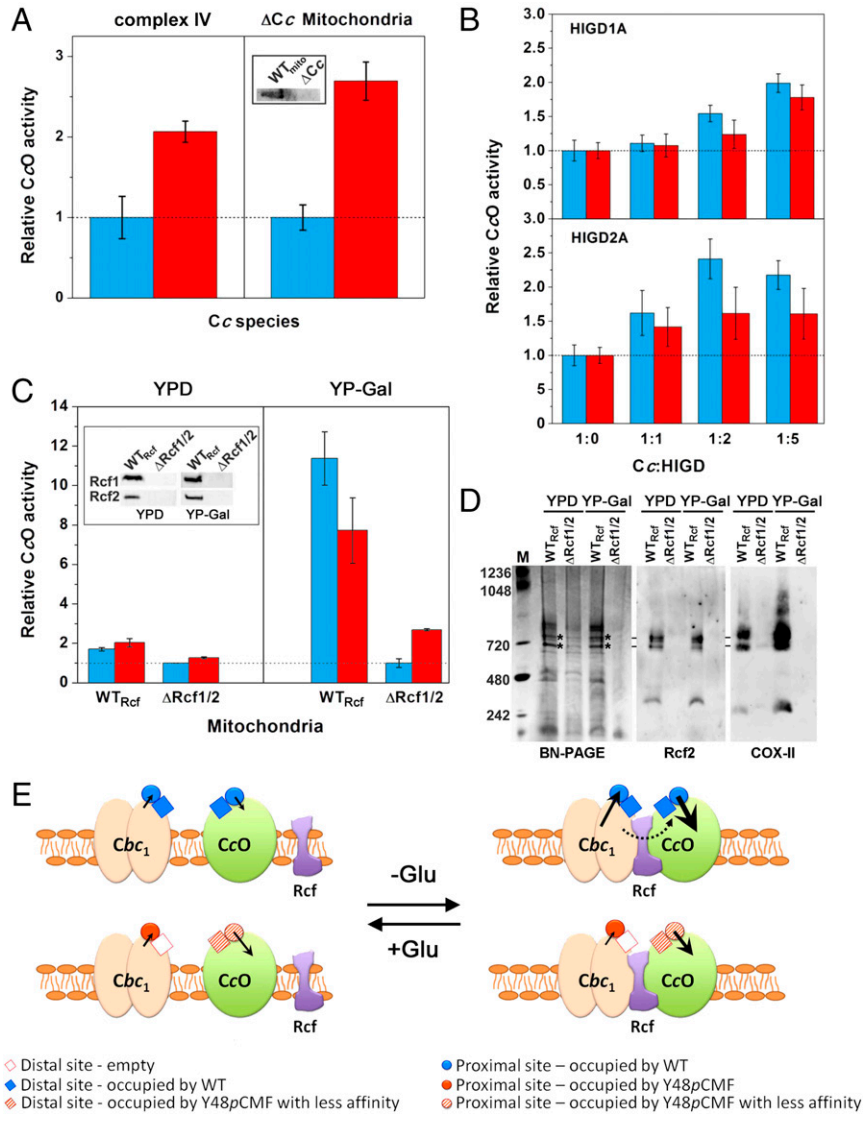

Fig. 5. CcO activity with WT or Y48*p*CMF Cc as the electron donor. (*A*) CcO activity of isolated complex IV and of mitochondria lacking Cc (ΔCc) upon addition of exogenous WT (blue bars) or Y48*p*CMF Cc (red bars). Western blot results confirmed the lack of endogenous Cc in ΔCc mitochondria (*Inset*). (*B*) In vitro modulation of CcO activity by HIGD1A and HIGD2A. WT Cc (blue bars) or Y48*p*CMF Cc (red bars), along with HIGD1A or HIGD2A at the indicated ratios, was added to isolated complex IV. (*C*) Effect of the modulators Rcf1 and Rcf2 on the CcO activity of mitochondria isolated from yeasts grown in YPD or YP-Gal media with either WT Cc (blue bars) or Y48*p*CMF Cc (red bars). All data represent the mean ± SD of three independent experiments. In all cases, CcO activity was detected only upon addition of exogenous Cc but not with endogenous Cc. (*C*, *Inset*) Western blots of WT_{Rcf} mitochondria (lane 1) and mitochondria lacking Rcf1 and Rcf2 (ΔRcf1/2) (lane 2). (*D*) BN/PAGE and Western blots of mitochondria from WT_{Rcf} and ΔRcf1/2 strains, using antibodies against Rcf2 and COX-II. Bands submitted to tryptic digestion (*SI Appendix*, Fig. S11*D*) are highlighted by asterisks. (*E*) Scheme of the interactions within the electron transport chain involving Cbc_1, CcO, Rcf proteins, and WT or Y48*p*CMF Cc, as a function of glucose (Glu) availability. The Rcf proteins facilitate the interaction between Cbc_1 and CcO to form OxPhos supercomplexes, mainly under glucose deprivation (*Right*). The thickness of solid arrows refers to the electron transfer rate at the Cc-binding proximal sites of Cbc_1 and CcO by WT or Y48*p*CMF Cc—the longer and thicker the arrow, the more efficient the electron transfer. The dashed line highlights the channeling of WT Cc molecules.

Tyr48-Phosphorylated Cytochrome *c* Acts as an Improved Peroxidase-Like Enzyme, in Particular When Bound to Cardiolipin-Containing Liposomes. Assembly of the mitochondrial protein membrane complexes Cbc_1 and CcO into OxPhos supercomplexes enables more efficient electron flow and decreases ROS levels generated by the ETC (63). The phospholipid CL, located in the inner mitochondrial membrane, also stabilizes the resulting supercomplexes (64) in a HIGD/Rcf-independent manner (59). In addition, CL interacts with Cc in a two-step binding reaction (65): In the first step, the so-called A site at the Cc surface makes transient electrostatic contacts with the membrane; in the second step, hydrophobic forces drive the formation of a tight and stable Cc–CL complex, with one of the CL acyl chains entering the hydrophobic groove of Cc (termed the C site) (66–68). C-site binding then triggers Cc-regulated CL peroxidation under oxidative stress and induces early apoptosis (40). Interestingly, several residues of Cc (Lys22, Lys27, and His33) become protonated at low pH to form an extra binding site—the so-called L site—that facilitates the electrostatic interaction of Cc with mitochondrial membranes (69).

Within this framework, we analyzed how tyrosine phosphorylation can fine-tune the affinity of Cc toward CL-containing liposomes, analyzing binding of Cc species to liposomes in Hepes buffer at a physiological pH value by electrophoretic mobility shift assays (EMSAs) in native agarose gels (Fig. 6 *A* and *B*). To compare the binding properties of Cc species to the CL-containing liposomes of 4:1 DOPC:TOCL (1,2-dioleoyl-*sn*-glycero-3-phosphocholine:1,1′,2,2′-tetraoleoylcardiolipin) or to liposomes of DOPC alone, we measured the mobility profiles of Cc at different Cc:lipid ratios. Although both WT and Y48*p*CMF Cc bound to DOPC:TOCL and DOPC vesicles, their binding affinity for the CL-free DOPC liposomes seemed to be lower (Fig. 6 *A* and *B*). Notably, the presence of free hemeprotein at high lipid concentrations suggested that Y48*p*CMF Cc has a lower affinity than WT toward DOPC:TOCL liposomes (Fig. 6*B*), as recently observed for the phosphomimetic mutant S47D Cc (70). Another interesting finding is the unspecific interaction of Cc—either the WT or Y48*p*CMF species—with DOPC vesicles (Fig. 6 *A* and *B*).

ITC measurements corroborated these EMSA data. ITC experiments were performed under aerobiosis to mimic physiological conditions, despite using degassed samples. This may result in partial oxidation of Cc upon binding to liposomes, as previously reported (71). ITC analysis yielded the apparent K_D values for the first binding event of 427 μM (WT Cc) and 780 μM (Y48*p*CMF Cc) (Fig. 6*C*). Data for the interaction of WT Cc with liposomes are consistent with the K_D values reported before (68, 72–74), but they diverge from the lower K_D values reported in the literature

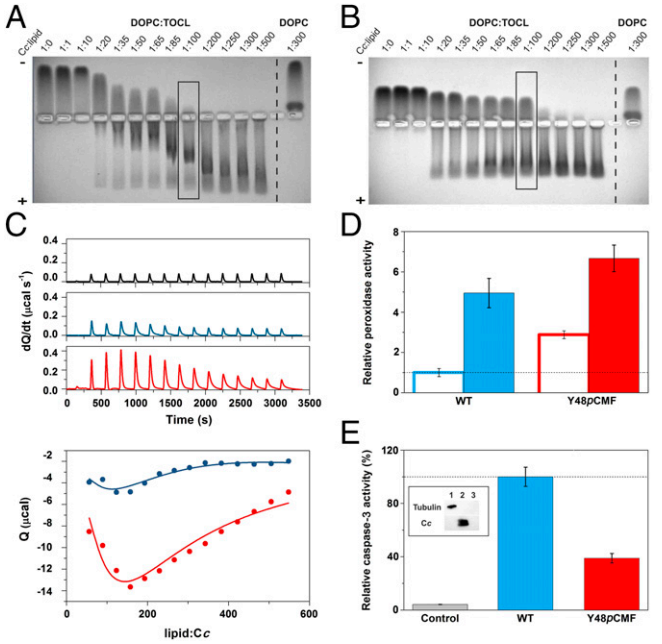

Fig. 6. Liposome-binding assays with caspase-3 activity induced by WT and Y48*p*CMF Cc. (*A* and *B*) EMSA of Cc in the presence of increasing concentrations of lipids. DOPC:TOCL (4:1) or DOPC liposomes were incubated with WT (*A*) or Y48*p*CMF (*B*) Cc. Note that free Cc species moved to the cathode, whereas liposome-bound Cc migrated to the anode. Lanes marked by rectangles correspond to the Cc:lipid ratio at which the peroxidase activity was determined (see below). (*C*) Calorimetric assays for lipid binding to Cc. (*C*, *Upper*) ITC thermograms, corresponding to titrations of DOPC:TOCL 4:1 liposomes (black), WT Cc (blue), or Y48*p*CMF Cc (red). (*C*, *Lower*) Binding isotherms with WT Cc (blue dots) or Y48*p*CMF Cc (red dots). Continuous lines represent the best fits to a sequential binding, as computed with NanoAnalyze software (TA Instruments) with a stoichiometry of 30 molecules of lipid per molecule of Cc. All data represent the mean ± SD of three independent experiments. (*D*) Relative peroxidase activities of WT Cc (blue) or Y48*p*CMF Cc (red) in the presence of liposomes containing DOPC (empty bars) or DOPC:TOCL (4:1) (filled bars). (*E*) Relative caspase-3 activity in HEK293 cell extracts devoid of endogenous Cc upon addition of exogenous WT Cc (blue) or Y48*p*CMF Cc (red). A lack of caspase autoactivation was verified in a run without the addition of Cc (gray). Western blots confirmed the lack of endogenous Cc in cytoplasmic cell extracts after immunoblotting with anti–α-tubulin (cytosolic marker) and anti-Cc antibodies (*Inset*). Lane 1, cytoplasmic cell extracts; lane 2, Cc; lane 3, BSA as a negative control. All data represent the mean ± SD of three independent experiments.

(75) and the A/C two-site binding model described by Kinnunen and coworkers (66, 67). Such discrepancies are still unresolved, and further research is necessary to harmonize data from all these different binding assays in a unified and single model. The interaction with CL resulted in apparent ΔH values equal to 2.75 kcal·mol^{-1} for WT Cc and 38.97 kcal·mol^{-1} for Y48*p*CMF Cc. The differences in K_D indicate a small change in binding energies (of ∼6 kcal·mol^{-1}). Hence, the changes in ΔH are indicative of enthalpy–entropy compensation effects, which are compatible with the electrostatic change resulting from the extra carboxylate group of the Y48*p*CMF species. Further, an exothermic process can be observed, with longer peak equilibrium times upon successive lipid additions. In this case, the apparent ΔH values with the WT and Y48*p*CMF Cc species were equal to −6.97 and −47.84 kcal·mol^{-1}, respectively, but the apparent K_D value (of ∼1 mM) was practically the same with the two Cc species. Altogether, our EMSA and ITC assays indicate that Y48*p*CMF Cc binds to CL-containing liposomes with a slightly lower affinity than WT Cc.

WT Cc undergoes CL-dependent conformational changes that allow H_2O_2 to access the heme crevice (74). Hence, we addressed whether the affinity differences between WT and Y48*p*CMF Cc for CL could affect their peroxidase activity. In the absence of CL-containing liposomes, Y48*p*CMF Cc exhibited a threefold higher peroxidase activity than WT Cc (Fig. 6*D*). However, the presence of DOPC:TOCL vesicles, at a 1:100 Cc:lipid ratio, increased the enzymatic activity of both WT and Y48*p*CMF Cc, similar to that observed for other phosphomimetic Cc mutants (70). Note that the slightly lower peroxidase activity increment observed for Y48*p*CMF Cc is likely due to its higher population of free protein compared with WT Cc (Fig. 6 *B* and *D*).

Tyr48 Phosphorylation Is an Antiapoptotic Posttranslational Modification. Phosphorylated Cc may be more easily released from mitochondria because of its lower affinity toward CL, as inferred from EMSA and ITC assays. Translocation to the cytosol could thus enable phosphorylated Cc to interact with Apaf-1 and to assemble the caspase-activating apoptosome. However, cytosolic caspase-3 activation was decreased by about 60% in the presence of the Y48*p*CMF Cc mutant (Fig. 6*E*). This is in agreement with the behavior previously reported for the Y48E Cc mutant, which exhibits a lower ability than WT Cc to activate not only caspase-3 (26) but also procaspase-9 by nonfunctional apoptosome assembly (27). These results could thus be indicative of an antiapoptotic function of Cc when phosphorylated at position 48.

Discussion

Here we tackle the structural and functional characterization of the Y48*p*CMF variant of human Cc. This mutation mimics protein phosphorylation at Tyr48 by adding a negative charge and slightly increasing the side-chain size while keeping the aromatic ring. A recent spectroscopic analysis of Y48*p*CMF Cc showed a singular shift of the typical alkaline transition pK_a to physiological pH values (31), as is the case with the Y48E Cc mutant (26, 27). Here, we report NMR-based structure computations that indicate that Tyr48 phosphorylation maintains the core foldon of Cc but increases internal motions in the loops Ω_{NY}, Ω_R, and Ω_G. Specifically, the Ω_{NY}-loop, the most unstable folding unit of the hemeprotein, becomes looser and reaches conformational equilibria in Y48*p*CMF Cc. Enhanced motions at the Ω_G- and Ω_R-loops could be associated with the shift in the alkaline transition pK_a. Indeed, these two loops hold the residues that provide the iron axial ligands, which are observed to at least partially lose their metal coordination in the alkaline form (76). This is in contrast to XAS data that suggest that axial coordination remains untouched. However, the cryogenic temperatures at which the XAS spectra were recorded may

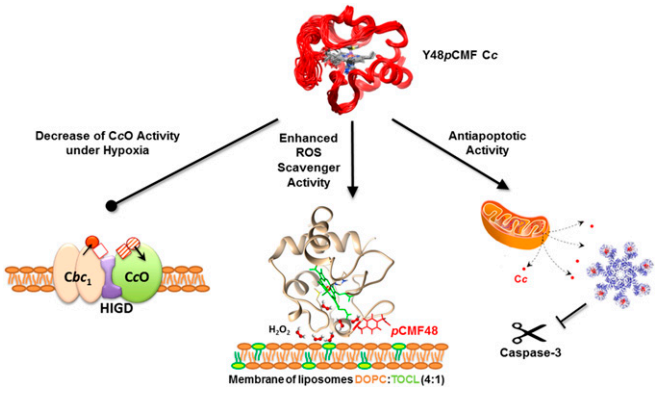

Fig. 7. Schematic diagram illustrating the changes induced in cell function by phosphomimetic Y48*p*CMF Cc. The negative charge at position 48 decreases CcO activity by disrupting Cc channeling in OxPhos supercomplexes (*Left*), enhances ROS scavenger activity by increasing the peroxidase activity of CL-bound Cc (*Middle*), and promotes the antiapoptotic function of Y48*p*CMF Cc by inhibiting its ability to activate the caspase-3 cascade (*Right*).

amplify the most stable structures and reduce contributions from minority species with a high disorder, which are undetectable.

The local but substantial changes in conformation and dynamics of the regions surrounding the Y48*p*CMF mutation increased the solvent accessibility of the porphyrin ring, thereby enhancing cytochrome peroxidase activity. Thus, Y48*p*CMF C*c* proficiently scavenges ROS and avoids damage of cellular components (Fig. 7). Our findings also indicate that Y48*p*CMF C*c* binds to mitochondrial CL with a lower affinity than WT C*c* but that Y48*p*CMF C*c* shows a higher peroxidase activity upon binding to liposomes. According to the literature, both events may facilitate C*c* translocation to the cytoplasm during apoptosis (77). However, phosphorylation at Tyr48 hinders the proapoptotic activity of extramitochondrial C*c*, similar to the function of HIGD1A protein in ischemia and tumorigenesis (78). Indeed, both HIGD1A and Y48*p*CMF C*c* act as prosurvival proteins by preventing apoptotic caspase activation (Fig. 7) (79).

As expected, the Y48*p*CMF mutation affects the binding mode of C*c* to its well-known respiratory partners Cbc_1 and C*c*O. Not surprisingly, the enhanced internal motions of the loops Ω_{NY} and Ω_R and the electrostatic change at the interaction patch resulting from the additional carboxyl group affect the interaction of Y48*p*CMF C*c* with the two membrane complexes. The mutation-induced changes in electrostatics and in solvation at the interface also concur for the interaction of reduced Y48*p*CMF C*c* with the distal sites of C*c*O (and Cc_1), as inferred from the high decrease in dissociation enthalpies and the strong (or moderate) enthalpy–entropy compensation herein reported. Indeed, the binding of Y48*p*CMF C*c* on the Cc_1 surface is weak and functionally irrelevant at the distal site but is favored at the proximal site (Fig. 5*E*). When the turnover of the redox carrier at the main site is considered, the high affinity of reduced Y48*p*CMF C*c* inhibits its own replacement by oxidized C*c* molecules, thereby impairing the electron transport.

The C*c*–C*c*O complex keeps its interface solvated, according to the recent X-ray diffraction structure (80), which displays a protruding lysine side chain in C*c*O pointing to Tyr48 in C*c*. A salt bridge involving phosphorylated Tyr48 would restrain the Ω_{NY}-loop. The increase in the K_D of the complex between Y48*p*CMF C*c* and C*c*O (this work) and the decrease in the Michaelis constant (K_M) of phosphorylated C*c* with C*c*O (81) indicate that K_M is mainly governed by the catalytic step. This agrees with the larger C*c*O-driven oxidation rate of Y48*p*CMF C*c* compared with that of WT C*c* at the limiting protein concentrations in the enzymatic activity assays used here. In this context, the ca. 60-mV decrease in the E_0 of Y48*p*CMF C*c* (31) may facilitate the electron flow from C*c* to C*c*O, although it may impair C*c* reduction by Cbc_1. In other words, Y48*p*CMF C*c* exhibits a reduced ability as oxidizing agent (it is less capable than WT C*c* of receiving electrons from Cc_1) but displays an increased capacity as reducing agent (it is a better electron donor to C*c*O than WT C*c*). It is well-known that the catalytic step can be tuned by conformational changes of C*c* upon binding to C*c*O (52). Strikingly, these changes resemble the prominent internal dynamics of Y48*p*CMF C*c*, which could also explain not only the change in E_0 but also the shift in the alkaline transition pK_a of oxidized Y48*p*CMF C*c* (31). Therefore, the transition from reduced to oxidized Y48*p*CMF C*c*, which is accompanied by a change in the iron axial ligand at physiological pH, is expected to have a high-energy barrier (82). Hence, such conformational changes might be the limiting step for Y48*p*CMF C*c* oxidation inside the complex.

Under nutrient and oxygen depletion, a dysfunctional mitochondrial ETC and OxPhos can lead to many human diseases, including pathologies such as ischemia and cancer (24). The nexus in both disorders could be the control of mitochondrial ET rate by C*c* phosphorylation (23), which has indeed been reported to efficiently fine-tune respiratory rates (81). Even though HIGD-mediated assembly of Cbc_1 and C*c*O into OxPhos supercomplexes preferably occurs under low-glucose conditions, the decrease in both the C*c*O activity and binding affinity toward Cc_1 and C*c*O resulting from the enhanced dynamics of Y48*p*CMF C*c* could explain the disruption of C*c* channeling inside the Cbc_1–C*c*O supercomplex, thus slowing down the ETC flow (Fig. 7).

Intriguingly, not only respiratory supercomplex formation (60, 61)—whose structure has recently been solved (83, 84)—but also C*c* phosphorylation, and the resulting decrease in the ETC rate, could help to keep ROS levels low and guarantee cell survival.

Tyr48-phosphorylated C*c* could be targeted as a biomarker of mitochondrial dysfunction for associated pathological states such as ischemia/reperfusion and cancer. Deciphering the details of the phosphorylated C*c*-controlled complex network requires accurate structural and dynamic analyses to eventually develop robust therapeutic approaches to foster or silence—as required—the prosurvival action of phosphorylated C*c* reported here.

Methods

Methods and associated references are available in *SI Appendix, Methods*. All biological samples were obtained from bacteria, yeast, or human cell extracts, in full compliance with University of Seville Ethical Committee bylaws.

ACKNOWLEDGMENTS. We acknowledge the NMR services at the Centro di Ricerca di Risonanze Magnetiche (CERM; Florence), Centro de Investigación, Tecnología e Investigación (CITIUS; Seville), and Biointeractomics Platform (BIP-cicCartuja; Seville), as well as TA Instruments. We also thank Diamond Light Source for access to beamline I20-scanning (Proposal SP-6011). Experimental work was performed in part at the Grenoble INSTRUCT Centre (ISBG; UMS 3518 CNRS-CEA-UJF-EMBL), with support from FRISBI (ANR-10-INSB-05-02) and GRAL (ANR-10-LABX-49-01) within the Grenoble Partnership for Structural Biology. Financial support was provided by the Spanish Ministry of Economy and Competitiveness (Grants BFU2015-71017-P/BMC and BFU2015-19451/BMC, cofounded by FEDER EU), European Union (Bio-NMR-00130 and CALIPSO-312284), Ramon Areces Foundation, and Andalusian Government (BIO198). B.M.-B. was awarded a PhD fellowship from the Spanish Ministry of Education (AP2009-4092) and a short-term traveling fellowship from the European Bio-NMR Project. A.G.-C. was awarded a PhD fellowship from the CSIC (JaePre-2011-01248).

1. Papa S (1982) Molecular mechanism of proton translocation by the cytochrome system and the ATPase of mitochondria. Role of proteins. *J Bioenerg Biomembr* 14: 69–86.
2. Turrens JF (2003) Mitochondrial formation of reactive oxygen species. *J Physiol* 552: 335–344.
3. Lenaz G, Genova ML (2010) Structure and organization of mitochondrial respiratory complexes: A new understanding of an old subject. *Antioxid Redox Signal* 12: 961–1008.
4. Ray PD, Huang BW, Tsuji Y (2012) Reactive oxygen species (ROS) homeostasis and redox regulation in cellular signaling. *Cell Signal* 24:981–990.
5. Hou T, Wang X, Ma Q, Cheng H (2014) Mitochondrial flashes: New insights into mitochondrial ROS signalling and beyond. *J Physiol* 592:3703–3713.
6. Solaini G, Baracca A, Lenaz G, Sgarbi G (2010) Hypoxia and mitochondrial oxidative metabolism. *Biochim Biophys Acta* 1797:1171–1177.
7. Lenaz G, et al. (2010) Mitochondrial respiratory chain super-complex I–III in physiology and pathology. *Biochim Biophys Acta* 1797:633–640.
8. Corcoran A, Cotter TG (2013) Redox regulation of protein kinases. *FEBS J* 280: 1944–1965.
9. Helling S, et al. (2012) Multiple phosphorylations of cytochrome *c* oxidase and their functions. *Proteomics* 12:950–959.
10. Díaz-Moreno I, García-Heredia JM, Díaz-Quintana A, De la Rosa MA (2011) Cytochrome *c* signalosome in mitochondria. *Eur Biophys J* 40:1301–1315.
11. Wegerich F, Turano P, Allegrozzi M, Möhwald H, Lisdat F (2009) Cytochrome *c* mutants for superoxide biosensors. *Anal Chem* 81:2976–2984.
12. Florence TM (1985) The degradation of cytochrome *c* by hydrogen peroxide. *J Inorg Biochem* 23:131–141.
13. Radi R, Thomson L, Rubbo H, Prodanov E (1991) Cytochrome *c*-catalyzed oxidation of organic molecules by hydrogen peroxide. *Arch Biochem Biophys* 288:112–117.
14. Radi R, Turrens JF, Freeman BA (1991) Cytochrome *c*-catalyzed membrane lipid peroxidation by hydrogen peroxide. *Arch Biochem Biophys* 288:118–125.
15. Martinou JC, Desagher S, Antonsson B (2000) Cytochrome *c* release from mitochondria: All or nothing. *Nat Cell Biol* 2:E41–E43.
16. Basova LV, et al. (2007) Cardiolipin switch in mitochondria: Shutting off the reduction of cytochrome *c* and turning on the peroxidase activity. *Biochemistry* 46: 3423–3434.

17. Kagan VE, et al. (2009) Cytochrome *c*/cardiolipin relations in mitochondria: A kiss of death. *Free Radic Biol Med* 46:1439–1453.
18. Bertini I, Chevance S, Del Conte R, Lalli D, Turano P (2011) The anti-apoptotic Bcl-x(L) protein, a new piece in the puzzle of cytochrome *c* interactome. *PLoS One* 6: e18329.
19. Martínez-Fábregas J, et al. (2013) New *Arabidopsis thaliana* cytochrome *c* partners: A look into the elusive role of cytochrome *c* in programmed cell death in plants. *Mol Cell Proteomics* 12:3666–3676.
20. Martínez-Fábregas J, et al. (2014) Structural and functional analysis of novel human cytochrome *c* targets in apoptosis. *Mol Cell Proteomics* 13:1439–1456.
21. González-Arzola K, et al. (2015) Structural basis for inhibition of the histone chaperone activity of SET/TAF-Iβ by cytochrome *c*. *Proc Natl Acad Sci USA* 112: 9908–9913.
22. Martínez-Fábregas J, Díaz-Moreno I, González-Arzola K, Díaz-Quintana A, De la Rosa MA (2014) A common signalosome for programmed cell death in humans and plants. *Cell Death Dis* 5:e1314.
23. Hüttemann M, et al. (2008) Regulation of oxidative phosphorylation, the mitochondrial membrane potential, and their role in human disease. *J Bioenerg Biomembr* 40: 445–456.
24. Hüttemann M, Lee I, Grossman LI, Doan JW, Sanderson TH (2012) Phosphorylation of mammalian cytochrome *c* and cytochrome *c* oxidase in the regulation of cell destiny: Respiration, apoptosis, and human disease. *Adv Exp Med Biol* 748:237–264.
25. Kadenbach B (1968) Incorporation of ^{32}P-phosphate into phosphatides of rat liver mitochondria in vivo and in vitro. *FEBS Lett* 2:118–120.
26. Pecina P, et al. (2010) Phosphomimetic substitution of cytochrome *c* tyrosine 48 decreases respiration and binding to cardiolipin and abolishes ability to trigger downstream caspase activation. *Biochemistry* 49:6705–6714.
27. García-Heredia JM, et al. (2011) Tyrosine phosphorylation turns alkaline transition into a biologically relevant process and makes human cytochrome *c* behave as an anti-apoptotic switch. *J Biol Inorg Chem* 16:1155–1168.
28. Díaz-Moreno I, García-Heredia JM, Díaz-Quintana A, Teixeira M, De la Rosa MA (2011) Nitration of tyrosines 46 and 48 induces the specific degradation of cytochrome *c* upon change of the heme iron state to high-spin. *Biochim Biophys Acta* 1807: 1616–1623.
29. García-Heredia JM, et al. (2012) Specific nitration of tyrosines 46 and 48 makes cytochrome *c* assemble a non-functional apoptosome. *FEBS Lett* 586:154–158.
30. Ly HK, et al. (2012) Perturbation of the redox site structure of cytochrome *c* variants upon tyrosine nitration. *J Phys Chem B* 116:5694–5702.
31. Guerra-Castellano A, et al. (2015) Mimicking tyrosine phosphorylation in human cytochrome *c* by the evolved tRNA synthetase technique. *Chemistry* 21:15004–15012.
32. Ripple MO, Abajian M, Springett R (2010) Cytochrome *c* is rapidly reduced in the cytosol after mitochondrial outer membrane permeabilization. *Apoptosis* 15: 563–573.
33. Jeng WY, Chen CY, Chang HC, Chuang WJ (2002) Expression and characterization of recombinant human cytochrome *c* in *E. coli*. *J Bioenerg Biomembr* 34:423–431.
34. Cornilescu G, Delaglio F, Bax A (1999) Protein backbone angle restraints from searching a database for chemical shift and sequence homology. *J Biomol NMR* 13: 289–302.
35. Baistrocchi P, et al. (1996) Three-dimensional solution structure of *Saccharomyces cerevisiae* reduced iso-1-cytochrome *c*. *Biochemistry* 35:13788–13796.
36. Banci L, Bertini I, Huber JG, Spyroulias GA, Turano P (1999) Solution structure of reduced horse heart cytochrome *c*. *J Biol Inorg Chem* 4:21–31.
37. Güntert P (2004) Automated NMR structure calculation with CYANA. *Methods Mol Biol* 278:353–378.
38. Laskowski RA, Rullmannn JA, MacArthur MW, Kaptein R, Thornton JM (1996) AQUA and PROCHECK-NMR: Programs for checking the quality of protein structures solved by NMR. *J Biomol NMR* 8:477–486.
39. Word JM, et al. (1999) Visualizing and quantifying molecular goodness-of-fit: Small-probe contact dots with explicit hydrogen atoms. *J Mol Biol* 285:1711–1733.
40. Rajagopal BS, et al. (2013) The hydrogen-peroxide-induced radical behaviour in human cytochrome *c*-phospholipid complexes: Implications for the enhanced pro-apoptotic activity of the G41S mutant. *Biochem J* 456:441–452.
41. Pettersen EF, et al. (2004) UCSF Chimera—A visualization system for exploratory research and analysis. *J Comput Chem* 25:1605–1612.
42. Karsisiotis AI, et al. (2016) Increased dynamics in the 40–57 Ω-loop of the G41S variant of human cytochrome *c* promote its pro-apoptotic conformation. *Sci Rep* 6: 30447.
43. Maity H, Maity M, Englander SW (2004) How cytochrome *c* folds, and why: Submolecular foldon units and their stepwise sequential stabilization. *J Mol Biol* 343: 223–233.
44. Xiao Y, et al. (2014) Phosphorylation releases constraints to domain motion in ERK2. *Proc Natl Acad Sci USA* 111:2506–2511.
45. Wauer T, et al. (2015) Ubiquitin Ser65 phosphorylation affects ubiquitin structure, chain assembly and hydrolysis. *EMBO J* 34:307–325.
46. Dosset P, Hus JC, Blackledge M, Marion D (2000) Efficient analysis of macromolecular rotational diffusion from heteronuclear relaxation data. *J Biomol NMR* 16:23–28.
47. Moreno-Beltrán B, et al. (2015) Respiratory complexes III and IV can each bind two molecules of cytochrome *c* at low ionic strength. *FEBS Lett* 589:476–483.
48. Moreno-Beltrán B, et al. (2014) Cytochrome c_1 exhibits two binding sites for cytochrome *c* in plants. *Biochim Biophys Acta* 1837:1717–1729.
49. Díaz-Moreno I, et al. (2005) NMR analysis of the transient complex between membrane photosystem I and soluble cytochrome c_6. *J Biol Chem* 280:7925–7931.
50. Díaz-Moreno I, Díaz-Quintana A, Ubbink M, De la Rosa MA (2005) An NMR-based docking model for the physiological transient complex between cytochrome *f* and cytochrome c_6. *FEBS Lett* 579:2891–2896.
51. Volkov AN, Worrall JA, Holtzmann E, Ubbink M (2006) Solution structure and dynamics of the complex between cytochrome *c* and cytochrome *c* peroxidase determined by paramagnetic NMR. *Proc Natl Acad Sci USA* 103:18945–18950.
52. Sakamoto K, et al. (2011) NMR basis for interprotein electron transfer gating between cytochrome *c* and cytochrome *c* oxidase. *Proc Natl Acad Sci USA* 108:12271–12276.
53. Boffi F, et al. (2001) pH-dependent local structure of ferricytochrome *c* studied by X-ray absorption spectroscopy. *Biophys J* 80:1473–1479.
54. Osheroff N, et al. (1983) The reaction of primate cytochromes *c* with cytochrome *c* oxidase. Analysis of the polarographic assay. *J Biol Chem* 258:5731–5738.
55. Garber EA, Margoliash E (1990) Interaction of cytochrome *c* with cytochrome *c* oxidase: An understanding of the high- to low-affinity transition. *Biochim Biophys Acta* 1015:279–287.
56. Speck SH, Margoliash E (1984) Characterization of the interaction of cytochrome *c* and mitochondrial ubiquinol-cytochrome *c* reductase. *J Biol Chem* 259:1064–1072.
57. Klammt C, et al. (2012) Facile backbone structure determination of human membrane proteins by NMR spectroscopy. *Nat Methods* 9:834–839.
58. Hayashi T, et al. (2015) Higd1a is a positive regulator of cytochrome *c* oxidase. *Proc Natl Acad Sci USA* 112:1553–1558.
59. Strogolova V, Furness A, Robb-McGrath M, Garlich J, Stuart RA (2012) Rcf1 and Rcf2, members of the hypoxia-induced gene 1 protein family, are critical components of the mitochondrial cytochrome bc_1-cytochrome *c* oxidase supercomplex. *Mol Cell Biol* 32:1363–1373.
60. Chen YC, et al. (2012) Identification of a protein mediating respiratory supercomplex stability. *Cell Metab* 15:348–360.
61. Vukotic M, et al. (2012) Rcf1 mediates cytochrome oxidase assembly and respirasome formation, revealing heterogeneity of the enzyme complex. *Cell Metab* 15: 336–347.
62. Fukuda R, et al. (2007) HIF-1 regulates cytochrome oxidase subunits to optimize efficiency of respiration in hypoxic cells. *Cell* 129:111–122.
63. Louro RO, Díaz-Moreno I, eds (2015) *Redox Proteins in Supercomplexes and Signalosomes* (CRC Press, Oxfordshire, UK).
64. Zhang M, Mileykovskaya E, Dowhan W (2002) Gluing the respiratory chain together. Cardiolipin is required for supercomplex formation in the inner mitochondrial membrane. *J Biol Chem* 277:43553–43556.
65. Belikova NA, et al. (2006) Peroxidase activity and structural transitions of cytochrome *c* bound to cardiolipin-containing membranes. *Biochemistry* 45:4998–5009.
66. Rytömaa M, Mustonen P, Kinnunen PK (1992) Reversible, nonionic, and pH-dependent association of cytochrome *c* with cardiolipin-phosphatidylcholine liposomes. *J Biol Chem* 267:22243–22248.
67. Rytömaa M, Kinnunen PK (1994) Evidence for two distinct acidic phospholipid-binding sites in cytochrome *c*. *J Biol Chem* 269:1770–1774.
68. Sinibaldi F, et al. (2008) Insights into cytochrome *c*-cardiolipin interaction. Role played by ionic strength. *Biochemistry* 47:6928–6935.
69. Kawai C, et al. (2005) pH-dependent interaction of cytochrome *c* with mitochondrial mimetic membranes: The role of an array of positively charged amino acids. *J Biol Chem* 280:34709–34717.
70. Guerra-Castellano A, Díaz-Moreno I, Velázquez-Campoy A, De la Rosa MA, Díaz-Quintana A (2016) Structural and functional characterization of phosphomimetic mutants of cytochrome *c* at threonine 28 and serine 47. *Biochim Biophys Acta* 1857: 387–395.
71. Serpas L, Milorey B, Pandiscia LA, Addison AW, Schweitzer-Stenner R (2016) Autoxidation of reduced horse heart cytochrome *c* catalyzed by cardiolipin-containing membranes. *J Phys Chem B* 120:12219–12231.
72. Hanske J, et al. (2012) Conformational properties of cardiolipin-bound cytochrome *c*. *Proc Natl Acad Sci USA* 109:125–130.
73. Pandiscia LA, Schweitzer-Stenner R (2015) Coexistence of native-like and non-native partially unfolded ferricytochrome *c* on the surface of cardiolipin-containing liposomes. *J Phys Chem B* 119:1334–1349.
74. Pandiscia LA, Schweitzer-Stenner R (2015) Coexistence of native-like and non-native cytochrome *c* on anionic liposomes with different cardiolipin content. *J Phys Chem B* 119:12846–12859.
75. Domanov YA, Molotkovsky JG, Gorbenko GP (2005) Coverage-dependent changes of cytochrome *c* transverse location in phospholipid membranes revealed by FRET. *Biochim Biophys Acta* 1716:49–58.
76. Assfalg M, et al. (2003) Structural model for an alkaline form of ferricytochrome *c*. *J Am Chem Soc* 125:2913–2922.
77. Kagan VE, et al. (2006) The "pro-apoptotic genies" get out of mitochondria: Oxidative lipidomics and redox activity of cytochrome *c*/cardiolipin complexes. *Chem Biol Interact* 163:15–28.
78. Ameri K, et al. (2015) HIGD1A regulates oxygen consumption, ROS production, and AMPK activity during glucose deprivation to modulate cell survival and tumor growth. *Cell Reports* 10:891–899.
79. An HJ, et al. (2011) The survival effect of mitochondrial *Higd-1a* is associated with suppression of cytochrome *c* release and prevention of caspase activation. *Biochim Biophys Acta* 1813:2088–2098.
80. Shimada S, et al. (2017) Complex structure of cytochrome *c*-cytochrome *c* oxidase reveals a novel protein-protein interaction mode. *EMBO J* 36:291–300.
81. Yu H, Lee I, Salomon AR, Yu K, Hüttemann M (2008) Mammalian liver cytochrome *c* is tyrosine-48 phosphorylated in vivo, inhibiting mitochondrial respiration. *Biochim Biophys Acta* 1777:1066–1071.
82. Blouin C, Guillemette JG, Wallace CJA (2001) Resolving the individual components of a pH-induced conformational change. *Biophys J* 81:2331–2338.
83. Gu J, et al. (2016) The architecture of the mammalian respirasome. *Nature* 537:639–643.
84. Letts JA, Fiedorczuk K, Sazanov LA (2016) The architecture of respiratory supercomplexes. *Nature* 537:644–648.